The Astrophysical Journal, 609:231–242, 2004 July 1

METHANOL IN W3(H_2O) AND SURROUNDING REGIONS

E. C. Sutton,[1] A. M. Sobolev,[2] S. V. Salii,[2] A. V. Malyshev,[2] A. B. Ostrovskii,[2] and I. I. Zinchenko[3]

Received 2003 October 25; accepted 2004 March 11

ABSTRACT

We present the results of an interferometric study of 38 millimeter-wave lines of $^{12}CH_3OH$ in the vicinity of the massive star-forming region W3(OH/H_2O). These lines cover a wide range of excitation energies and line strengths, allowing for a detailed study of excitation mechanisms and opacities. In this paper we concentrate on the region around the water maser source W3(H_2O) and a region extending about 30″ to the south and west of the hydroxyl maser source W3(OH). The methanol-emitting region around W3(H_2O) has an extent of $2\farcs0 \times 1\farcs2$ (4400×2600 AU). The density is of the order of 10^7 cm^{-3}, sufficient to thermalize most of the methanol lines. The kinetic temperature is approximately 140 K and the methanol fractional abundance greater than 10^{-6}, indicative of a high degree of grain mantle evaporation. The W3(H_2O) source contains substructure, with peaks corresponding to the TW source and, separated from it by 2500 AU in projection, a combination of Wyrowski's sources B and C. The kinematics is consistent with these being distinct protostellar cores in a wide binary orbit and a dynamical mass for the region of a few tens of $M_\odot$. The extended methanol emission to the southwest of W3(OH) is seen strongly only from the lowest excitation lines and from lines known elsewhere to be Class I methanol masers, namely, the 84.5 GHz 5_{-1}–4_0E and 95.2 GHz 8_0–7_1A^+ lines. This suggests that this region, like Class I maser sources, is dominated by collisional excitation. Within this region there are two compact clumps, which we denote as swA and swB, each about 15″ (0.16 pc projected distance) away from W3(OH). Excitation analysis of these clumps indicates the presence of lines with inverted populations but only weak amplification. The sources swA and swB appear to have kinetic temperatures of the order of 50–100 K and densities of the order of 10^5–10^6 cm^{-3}. The methanol fractional abundance for the warmer clump is of the order of 10^{-7}, suggestive of partial grain mantle evaporation. The clumping occurs on mass scales of the order of 1 $M_\odot$.

Subject headings: ISM: clouds — ISM: individual (W3) — ISM: molecules — masers — radio lines: ISM

1. INTRODUCTION

Methanol is an abundant interstellar molecule, especially in regions of star formation, where its high abundance is thought to be the result of thermal evaporation of dust grain mantles (Caselli et al. 1993). A slightly asymmetric rotor with hindered internal rotation and significant *a*- and *b*-axis dipole moments, methanol has a complex spectrum that is sensitive to interstellar conditions. Observable lines cover a wide range of energies and line strengths, allowing for detailed analysis of excitation conditions and opacities.

Two classes of interstellar methanol masers are known. Class I methanol masers, produced by collisional pumping, are seen in regions of massive star formation but are generally well separated from the centers of activity as traced by embedded infrared sources and ultracompact H II (UCH II) regions. Class II methanol masers are thought to be produced by radiative excitation at infrared wavelengths and are spatially well correlated with young stellar objects, UCH II regions, and OH masers. Even when not masing, methanol may be expected to exhibit distinctly non-LTE excitation, except under the highest density conditions, where collisions could thermalize the level populations.

The southeastern portion of W3 contains the hydroxyl maser source W3(OH), which is associated with a UCH II region around a young O7 star, and the nearby water maser source W3(H_2O), which contains a young stellar object known as the TW object (Turner & Welch 1984). Numerous studies have been made of molecular material associated with these two compact objects and throughout the region surrounding them (Wilson et al. 1991, 1993; Wink et al. 1994; Helmich & van Dishoeck 1997; Wyrowski et al. 1999; Nilsson et al. 2000b). W3 is thought to be about 2.2 kpc from the Sun (Humphreys 1978). At such a distance, resolution of the order of 1″ is necessary to study the nature of protostellar cores on scales of the order of 1000 AU.

Sutton et al. (2001) presented results on new Class II methanol masers in W3(OH) and discussed excitation conditions needed to explain observed fluxes in those and several other methanol maser candidate lines. Sobolev et al. (2004) extended that analysis to include absorption and emission components in a larger set of methanol lines in W3(OH) and discussed the implications in terms of excitation and source structure. Here we wish to complete our analysis of methanol in the vicinity of W3(OH) and W3(H_2O) by presenting our complete set of millimeter-wave observations and by discussing the nature of the methanol associated with the W3(H_2O) source and methanol in other nearby regions.

2. OBSERVATIONS

Observations were carried out with the BIMA[4] interferometer between 1997 October and 2001 June, following the general procedures discussed in Sutton et al. (2001). The set of observed $^{12}CH_3OH$ transitions is presented in Table 1. In

[1] Department of Astronomy, University of Illinois, 1002 West Green Street, Urbana, IL 61801; sutton@astro.uiuc.edu.

[2] Astronomical Observatory, Ural State University, Lenin Street 51, Ekaterinburg 620083, Russia; andrej.sobolev@usu.ru; svetlana.salii@usu.ru; malyshev@ampural.ru; osan@mail.ur.ru.

[3] Institute of Applied Physics of the Russian Academy of Sciences, Ul. Ul'yanov 46, Nizhny Novgorod 603950, Russia; zin@appl.sci-nnov.ru.

[4] The Berkeley-Illinois-Maryland Association operates the BIMA array, under support from the National Science Foundation.

TABLE 1
OBSERVED $^{12}CH_3OH$ LINES

TRANSITION		FREQUENCY	E_u	μ^2S	BEAM
Line	State	(MHz)	(K)	(D^2)	(arcsec^2)
$7_2-8_1A^-$		80,993.26	103	2.52	2.6×2.5
$13_{-3}-14_{-2}E$		84,423.71	274	4.30	2.5×2.4
$5_{-1}-4_0E$		84,521.21	40	3.08	2.5×2.4
$6_{-2}-7_{-1}E$		85,568.07	75	2.01	3.7×2.7
$7_2-6_3A^-$		86,615.60	103	1.36	2.0×1.7
$7_2-6_3A^+$		86,902.95	103	1.36	2.0×1.8
$8_{-4}-9_{-3}E$		89,505.78	171	1.56	3.6×2.6
1_0-2_1E	$v_t = 1$	93,196.66	303	1.34	2.3×2.1
8_3-9_2E		94,541.81	131	2.24	2.8×2.2
$8_0-7_1A^+$		95,169.52	84	7.22	2.5×2.2
$2_1-1_1A^+$	$v_t = 1$	96,396.06	332	1.21	2.1×1.9
2_1-1_1E	$v_t = 1$	96,492.16	298	1.21	2.1×1.9
2_0-1_0E	$v_t = 1$	96,493.55	308	1.62	2.1×1.9
$2_{-1}-1_{-1}E$	$v_t = 1$	96,501.70	420	1.21	2.1×1.9
$2_0-1_0A^+$	$v_t = 1$	96,513.67	431	1.62	2.1×1.9
$2_1-1_1A^-$	$v_t = 1$	96,588.59	332	1.21	2.3×2.0
$2_{-1}-1_{-1}E$		96,739.36	12.5	1.21	2.1×1.8
$2_0-1_0A^+$		96,741.38	7.0	1.62	2.1×1.8
2_0-1_0E		96,744.55	20	1.62	2.1×1.8
2_1-1_1E		96,755.51	28	1.24	2.1×1.8
6_1-5_0E	$v_t = 1$	99,730.96	340	3.14	2.1×1.8
13_2-12_3E		100,638.87	234	3.84	3.2×2.4
$13_{-3}-12_{-4}E$		104,060.72	274	3.27	3.7×2.5
$11_{-1}-10_{-2}E$		104,300.40	159	3.41	3.1×2.3
$13_{-2}-13_1E$		104,336.64	237	1.20	2.9×1.5
$10_4-11_3A^-$		104,354.86	208	2.48	3.1×2.3
$10_4-11_3A^+$		104,410.49	208	2.48	3.1×2.3
$13_1-12_2A^+$		105,063.76	224	4.27	2.3×1.9
$14_{-2}-14_1E$		105,576.39	270	1.79	2.3×1.9
$3_1-4_0A^+$		107,013.81	28	3.01	1.6×1.4
$15_{-2}-15_1E$		107,159.92	305	2.61	1.8×1.6
$0_0-1_{-1}E$		108,893.93	13.1	0.98	2.2×1.8
14_5-15_4E		109,138.69	380	3.41	2.2×1.9
$16_{-2}-16_1E$		109,153.21	342	3.68	2.2×1.8
$7_2-8_1A^+$		111,289.60	103	2.34	1.9×1.6
5_1-4_2E		216,945.56	56	1.12	2.5×2.3
$6_1-7_2A^-$	$v_t = 1$	217,299.16	374	4.66	2.5×2.3
8_0-7_1E		220,078.49	97	3.45	2.4×2.2

NOTE.—Data are from Xu & Lovas (1997), except the 107,103.81 MHz line, for which the data are from Tsunekawa et al. (1995).

addition, observations were made of the central four lines of the $J = 2-1$ band of $^{13}CH_3OH$. At 3 mm, the data were primarily from the BIMA B- and C-arrays, with a small amount of A-array data for two of the lines. At 1 mm, the data were from the BIMA C- and D-arrays. In all cases spatial resolution was of the order of $2''$, as shown in Table 1. Spectral resolution was generally of the order of 0.2 km s^{-1}, although some observations were made with resolution as wide as 1.2 km s^{-1}. The continuum was subtracted from the u-v data before maps were made. The phase center of the maps is $\alpha(\mathrm{J2000.0}) = 2^{\mathrm{h}}27^{\mathrm{m}}03^{\mathrm{s}}.87$, $\delta(\mathrm{J2000.0}) = 61^\circ52'24''.6$. The flux density scale is thought to be accurate to within about $\pm10\%$ for the 3 mm band and about $\pm25\%$ for the 1 mm band.

In order to check for spatially extended emission, the 96.7 GHz methanol $J = 2-1$ band also was mapped using the 20 m Onsala telescope during 1998 January. The BIMA $J = 2-1$ maps and the Onsala maps are in general agreement with regard to the extent and shape of the emitting region. Furthermore, the BIMA interferometer maps recover about 75% of the peak flux density of these lines in the Onsala data. These lines are among the lowest energy lines in our data set and therefore more likely to be excited in diffuse, spatially extended material. Since we appear to have recovered most of the flux in these low-energy lines, we believe that we likely have also done so for the remaining lines in our data set. Since the BIMA maps have considerably higher spatial resolution and positional accuracy, and since we only have Onsala data for 4 of our 38 lines, in the discussion that follows we treat the BIMA maps by themselves, without further reference to the Onsala data.

3. RESULTS

3.1. *Low-Energy Lines*

In Figure 1 we show maps from those methanol lines we have measured that have upper-state energies of less than 100 K and for which we have u-v data that are substantially complete down to spatial frequencies of 3 kλ or less. In other

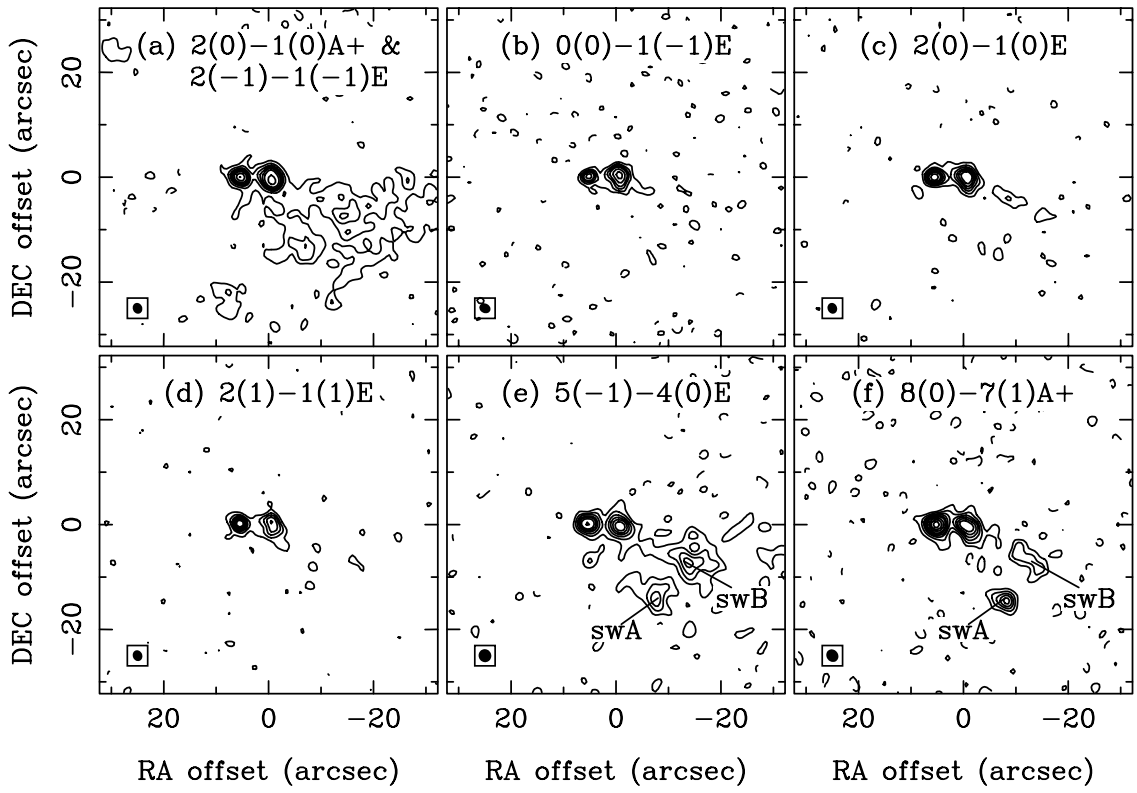

FIG. 1.—Emission from lines with upper-state energies less than 100 K for which data are available down to spatial frequencies of 3 kλ or less. Lines are presented in order of increasing upper-state energy. The map center is α(J2000.0) = $2^h27^m03^s.87$, δ(J2000.0) = $61°52'24''.6$, the nominal position of W3(OH). Sutton et al. (2001) found the 3 mm continuum from the W3(OH) UC H II region to peak $0''.2 \pm 0''.1$ west of this position. The TW object is $5''.94$ east of the phase center (Wyrowski et al. 1999; Reid et al. 1995). With the exception of (*a*), the plots are of average intensity over a v_{lsr} range of −53 to −42 km s^{-1}. A blend of lines is shown in (*a*), and the intensity is an average over a range of channels corresponding to −52.3 km s^{-1} for the 2_0–1_0A^+ line to −41.6 km s^{-1} for the 2_{-1}–$1_{-1}E$ line. Beams are shown in the lower left corners of the plots, and their sizes are listed in Table 1. Contours are 0.05, 0.1, 0.15, 0.2, 0.25, 0.3, 0.4, 0.5, and 0.6 Jy beam^{-1} for (*a*), (*c*), (*d*), (*e*), and (*f*) and 0.075, 0.15, 0.225, 0.3, 0.4, 0.5, and 0.6 Jy beam^{-1} for (*b*).

words, these maps are based on data sufficient to show any large-scale structure that might be present. Diffuse emission is present from spatially extended material to the southwest of W3(OH). This southwest region is discussed in detail in § 4.1, below.

3.2. *Other a-Type Lines*

In addition to the four $J = 2$–1 lines from the ground torsional state, shown in Figures 1*a*, 1*c*, and 1*d*, we also observed all six lines from the $J = 2$–1 band in the first torsionally excited state ($v_t = 1$). The torsionally excited lines are shown in Figure 2. These lines have upper-state energies of the order of 300–400 K and highlight the high-excitation material in the vicinity of the two main sources of luminosity, W3(OH) and W3(H_2O). Taken together, these 10 *a*-type lines from the $v_t = 0$, 1 states form a standard against which other methanol lines can be compared, since the *a*-type lines are less affected by non-LTE conditions than the 28 *b*-type lines discussed below.

We also observed the 2_0–1_0A^+, 2_{-1}–$1_{-1}E$, 2_0–1_0E, and 2_1–1_1E lines of $^{13}CH_3OH$. All four lines are weak, but visible, toward both W3(OH) and W3(H_2O). Flux densities are consistent with $^{12}C/^{13}C$ isotopic ratios of the order of 60 and moderate opacities in the $^{12}CH_3OH$ lines, as discussed by A. M. Sobolev et al. (2004, in preparation) and in § 4.2, below.

3.3. *Other b-Type Lines*

In Figure 3 we present maps of 15 *b*-type methanol lines, in addition to the three *b*-type lines already presented in Figures 1*b*, 1*e*, and 1*f*. Many of these lines are expected to be strong under Class II (radiative pumping) conditions. These include the maser lines discussed in Sutton et al. (2001) (Figs. 3*a*, 3*f*, and 3*g*) and the maser candidate lines (Figs. 1*b*, 3*c*, 3*e*, 3*h*, 3*i*, and 3*l*) discussed in the same paper. Note the tendency for the emission to be stronger in these lines toward W3(OH) than toward W3(H_2O), with the exceptions of the 6_{-2}–$7_{-1}E$ line at 85.5 GHz and the 8_3–9_2E line at 94.5 GHz. Both of these lines are predicted to mase under some Class II conditions by Sobolev et al. (1997a), and the 85.5 GHz line has been seen masing in G345.01+1.79 (Sobolev et al. 1998). However, both lines were predicted to be in absorption under the specific conditions of high kinetic temperature derived by Sutton et al. (2001) for W3(OH).

Figure 3 also contains data on three new transitions expected to be strong under radiative pumping conditions. The 5_1–4_2E line (Fig. 3*b*) has recently been seen as a Class II maser in G345.01+1.79 by Sobolev et al. (2002), and indeed it is quite strong here in the vicinity of W3(OH), although there is no evidence of a narrow maser spike at −43.1 km s^{-1}, as was characteristic of the 86 and 107 GHz masers discussed by Sutton et al. (2001). However, the W3(OH) emission extending from about −48 to −43 km s^{-1} could be a superposition of a number of weak maser features, similar to the case of several maser candidate lines discussed in Sutton et al. (2001).

The other new lines expected to be strong under radiative pumping are torsionally excited lines, 1_0–2_1E $v_t = 1$ and 6_1–7_2A^- $v_t = 1$. These are particularly important in understanding the Class II maser excitation mechanism, since that

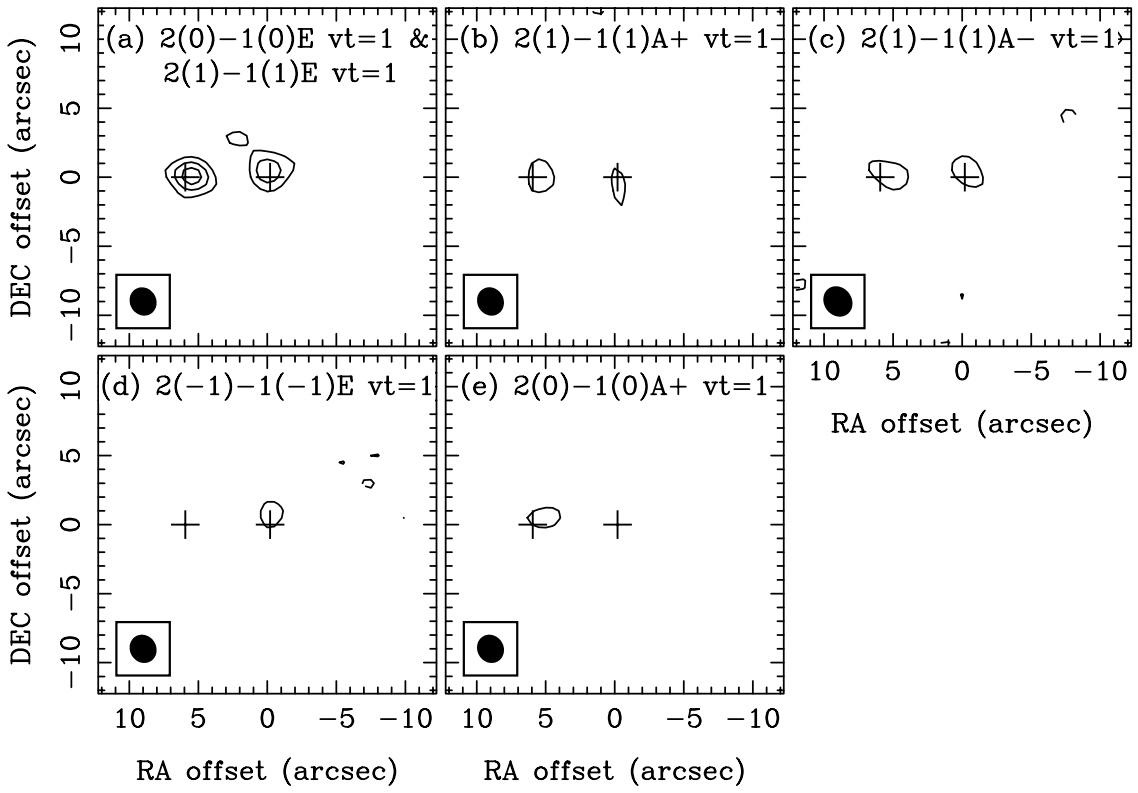

FIG. 2.—$J = 2-1$ lines from the first torsionally excited state. Map center and velocity range are the same as for Fig. 1. Beams are shown in the lower left corners of the plots, and their sizes are listed in Table 1. Symbols mark the positions of the TW object and the 3 mm continuum center of W3(OH). Contours are multiples of 0.05 Jy beam^{-1}.

mechanism involves radiative excitation through the first two torsionally excited bands of methanol, $v_t = 1$ and 2. Voronkov et al. (2002) recently observed the 2_0–3_1E $v_t = 1$ line at 44.9 GHz in several galactic sources and concluded that it is likely to be weakly masing in W3(OH). They predicted that the closely related 1_0–2_1E $v_t = 1$ 93.1 GHz line would also be inverted in W3(OH), and our observations (Fig. 3*m*) demonstrate strong emission in that direction. Calculations show that 6_1–7_2A^- $v_t = 1$ also is highly excited by the Class II mechanism and can be a weak maser (A. M. Sobolev et al. 2004, in preparation). We do not have enough evidence here to confirm masing in either of these lines. But the calculations mentioned above indicate superthermal excitation in both lines in the vicinity of W3(OH).

Other *b*-type lines are expected to be favored under Class I (collisional pumping) conditions. The 5_{-1}–4_0E and 8_0–7_1A^+ lines are discussed extensively in § 4.1. Here, in Figures 1*e* and 1*f*, we draw attention to the fact that emission from these lines is somewhat stronger from W3(H_2O) than from W3(OH). Data are presented on three other lines from the ground torsional state: 8_0–7_1E, 11_{-1}–$10_{-2}E$, and 13_1–12_2A^+ (Figs. 3*d*, 3*j*, and 3*k*, respectively). It is unclear how strongly 8_0–7_1E and 13_1–12_2A^+ might be favored by Class I conditions and disfavored by Class II conditions, although the data show that 13_1–12_2A^+ emission is indeed stronger toward W3(H_2O) than W3(OH). The 104.3 GHz 11_{-1}–$10_{-2}E$ line belongs to the same series as the 9.9 GHz Class I methanol maser 9_{-1}–$8_{-2}E$. To the best of our knowledge, the 9.9 GHz maser has been seen, weakly, in only one source, W33-Met (Slysh et al. 1993). Voronkov and Alakoz have recently seen maser emission in the 104.3 GHz line, again only in W33-Met (M. Voronkov 2003, private communication). Calculations reported by Cragg et al. (2001) suggest that the relative excitation of the $K = -1$ and $K = -2$ *E*-ladders is very model-dependent. Here we simply note that emission from 11_{-1}–$10_{-2}E$ is stronger toward W3(OH) than toward W3(H_2O). Finally, in Figure 3*n* we present data from a torsionally excited line, 6_1–5_0E $v_t = 1$, that should be more favored by Class I conditions than by Class II, and indeed it is stronger toward W3(H_2O) than W3(OH).

We have data on 10 other *b*-type lines, listed in Table 1 but not presented in Figures 1 or 3. Although these additional lines are used in the analysis that follows, either the maps have relatively poor sensitivity or the lines are not strongly preferred by either Class I or Class II conditions. For example, four of these lines are relatively high-*J* members of the J_{-2}–J_1E species *Q* branch. Most of the remaining lines in this category are of similarly high *J* or have $|K| \geq 3$. They are of minor importance in the analysis.

4. DISCUSSION

4.1. *Spatially Extended Material to the Southwest*

Some emission to the southwest of W3(OH) is visible in all of the lines shown in Figure 1, although it is most extensive in the lowest energy lines plotted in Figure 1*a*. This is a blend of the 2_0–1_0A^+ ($E_u = 7$ K) and 2_{-1}–$1_{-1}E$ ($E_u = 12.5$ K) lines. The relative weakness of the emission in this region for the other lines of the $J = 2-1$ band, 2_0–1_0E at $E_u = 20$ K (Fig. 1*c*) and 2_1–1_1E at $E_u = 28$ K (Fig. 1*d*), indicates that this is optically thin emission from low-excitation material. An average of the emission in the lower right quadrant of the plots for the $J = 2-1$ lines [excluding emission within 4″ of W3(OH) itself] implies a rotational temperature

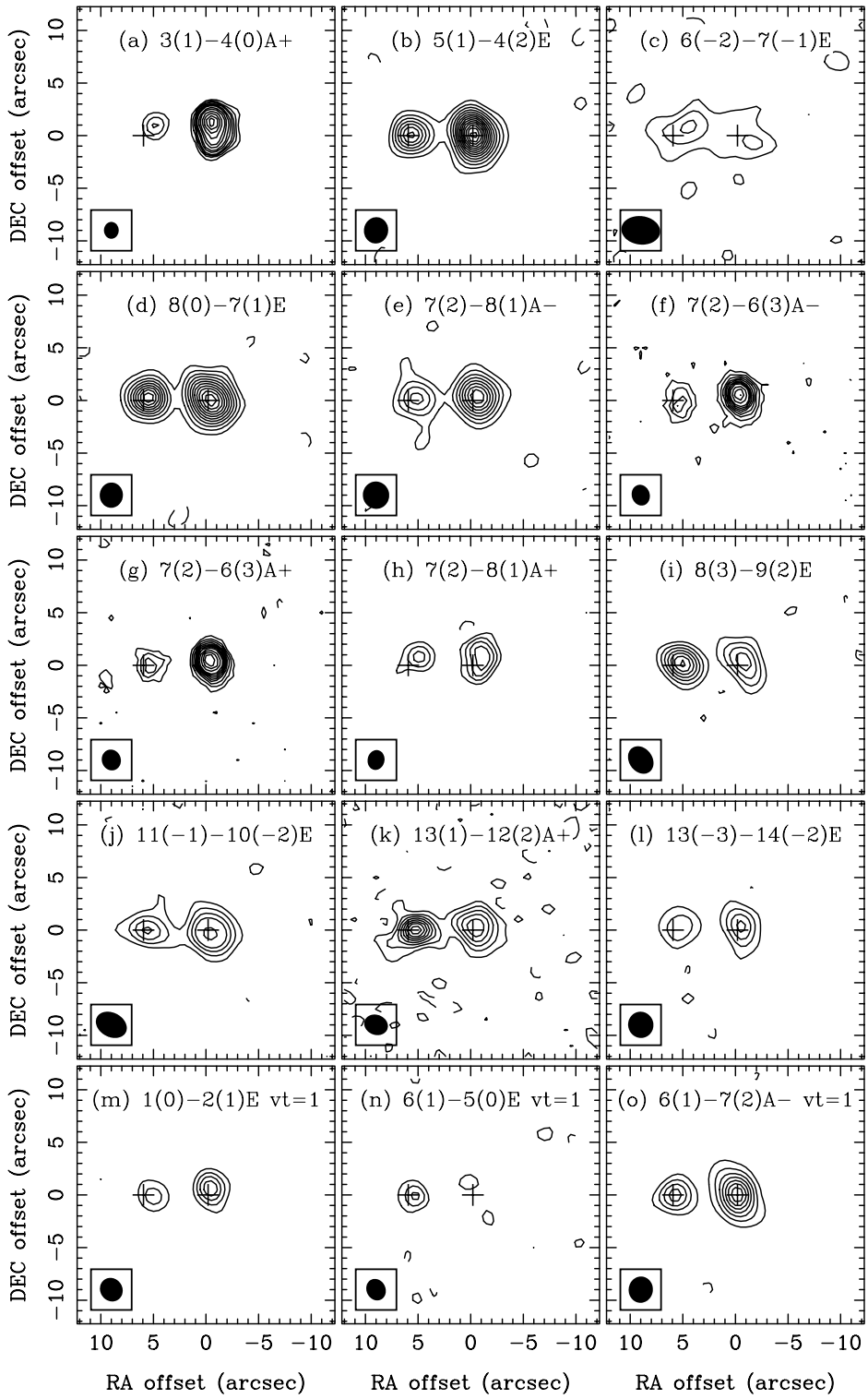

FIG. 3.—Maps of 15 *b*-type lines toward W3(OH)/W3(H_2O). Map center and velocity range are the same as for Fig. 1. Beams are shown in the lower left corners of the plots, and their sizes are listed in Table 1. Where space allows, symbols mark the positions of the TW object and the 3 mm continuum center of W3(OH). Contours are 0.05, 0.1, 0.15, . . . , 0.4, 0.5, 0.6, 0.7, and 0.8 Jy beam^{-1} for (*e*), (*f*), (*g*), (*i*), (*k*), (*l*), (*m*), and (*n*). Contours are 0.125, 0.25, 0.375, 0.5, 0.75, 1.0, 1.5, 2.0, and then multiples of 1 Jy beam^{-1} for (*a*), (*c*), (*h*), and (*j*). For (*b*), (*d*), and (*o*), the contours are multiples of 0.25 Jy beam^{-1}.

of 11 K. This is consistent with a kinetic temperature of the order of 50 K and a density of the order of 10^5–10^6 cm^{-3} (more detailed calculations are given below). This methanol emission shows good spatial and kinematical correspondence with material to the southwest of W3(OH) seen in NH_3 (1, 1) and (2, 2) emission by Wilson et al. (1993), who find the gas in that region to be characterized by a hydrogen density of 6×10^5 cm^{-3} and a rotational temperature of 30 K. It appears that in methanol we are seeing material similar to that seen in metastable ammonia. The presence of high-density material in this region is also suggested by the SO and CS data of Nilsson et al. (2000a).

TABLE 2
DATA FOR CLUMPS swA AND swB

Transition	v_{LSR} (km s^{-1})	Δv (km s^{-1})	S_{peak} (Jy)	$\int S_\nu\, dv$ (Jy km s^{-1})	Model (Jy km s^{-1})
		Clump swA			
2_0–1_0A^+	−45.9	3.3	1.8	6.0 ± 0.6	5.7
2_{-1}–$1_{-1}E$	−45.9	3.6	1.4	5.1 ± 0.5	4.9
0_0–$1_{-1}E$	−46.7	4.6	0.4	1.6 ± 0.3	0.8
2_0–1_0E	−46.3	3.4	0.6	2.0 ± 0.2	2.3
2_1–1_1E	−46.3	3.1	0.3	1.0 ± 0.2	0.4
5_{-1}–4_0E	−45.8	2.1	2.2	5.3 ± 0.5	5.0
8_0–7_1A^+	−46.4	2.5	2.0	5.2 ± 0.5	5.6
		Clump swB			
2_0–1_0A^+	−46.4	2.8	3.1	9.5 ± 1.0	8.1
2_{-1}–$1_{-1}E$	−46.6	2.5	2.5	6.7 ± 0.7	6.5
0_0–$1_{-1}E$	−46.6	2.4	1.4	3.6 ± 0.4	3.2
2_0–1_0E	−46.4	2.3	1.8	4.3 ± 0.4	5.1
2_1–1_1E	−46.4	2.3	1.0	2.4 ± 0.3	2.1
5_{-1}–4_0E	−46.4	2.2	4.0	9.4 ± 1.0	4.5
8_0–7_1A^+	−46.2	2.7	2.2	6.1 ± 0.6	6.7

Within the low-excitation methanol region are two clumps that show up prominently in the 5_{-1}–4_0E and 8_0–7_1A^+ lines. These are the clumps labeled swA and swB in Figures 1*e* and 1*f*, at offsets of ($\Delta\alpha = -8''$, $\Delta\delta = -14''$) and ($\Delta\alpha = -13''$, $\Delta\delta = -7''$), respectively. Since W3(OH) itself is a Class II methanol maser source, the presence of strong compact emission in these lines, known for their strong *Class I* maser emission, is unexpected. It seems that in these two regions at least, the excitation conditions are more like those found in Class I sources. The Class I mechanism is driven by collisional pumping. Therefore, in the regions of clumps swA and swB, collisions evidently are producing superthermal excitation in these, and potentially other, Class I methanol maser lines, whereas radiative pumping is less important. These positions are also near local maxima in the 2_0–1_0A^+ and 2_{-1}–$1_{-1}E$ map (Fig. 1*a*). The Class I mechanism can also modestly enhance the intensity of these two particular $J = 2-1$ lines, although it seems likely that these positions are also local maxima in methanol column density.

To show that either of these regions is actually weakly masing via the Class I mechanism requires further evidence, such as subthermal line widths or brightness temperatures well in excess of conceivable kinetic temperatures. Data on line widths and flux densities from clumps swA and swB are contained in Table 2. The line widths are narrow (2–3 km s^{-1} FWHM for the $5_{-1}-4_0E$ and $8_0-7_1A^+$ lines), but not sufficiently so as to conclude that these are masers (line widths of Class II masers in this source are typically 0.3 km s^{-1}, and thermal widths at 50 K are of a similar order).

Emission is strong and compact for clump swA in the $8_0-7_1A^+$ line, so this would seem to be the best case for making an argument in favor of maser emission based on brightness. The spatial resolution of the map shown in Figure 1*f* is $2\farcs5 \times 2\farcs2$. Clump swA is partially resolved in this map. On the basis of a deconvolved source size of $3\farcs0 \times 1\farcs9$ and a peak flux density of 2.0 Jy, we derive a brightness temperature of 48 K. If structure is present at spatial scales smaller than the current resolution, this represents a lower limit on the brightness. This is not sufficient to prove Class I maser action, but since this temperature is greater than that known for other material to the southwest of W3(OH) and there is no known source of luminosity near this position, it seems likely that some degree of maser amplification is taking place. The alternative, that this is simply a high-density clump in otherwise rather warm material, seems unlikely because of the weakness of the 2_0–1_0E and 2_1–1_1E emission in this region.

The remaining line to be discussed in this context is 0_0–$1_{-1}E$, presented as Figure 1*b*. In this transition we see relatively little emission at the locations of clumps swA and swB, as well as throughout the region to the southwest of W3(OH), even though the upper-state energy of this transition is only 13.1 K. The reason for this appears to be that this line is favored by Class II excitation conditions and is a known Class II maser in G345.01+1.79 (Val'tts et al. 1999). Lines that mase or are superthermally excited under Class II conditions are expected to be subthermally excited under Class I conditions, such as prevailing here to the southwest of W3(OH) and specifically near clumps swA and swB.

It might seem difficult to be precise about the conditions in these regions because of the small number of lines detected toward clumps swA and swB, the likely nonthermal nature of the excitation, and the possibility of significant opacity in the lowest energy lines. However, non-LTE fits to the data for these seven lines do provide significant constraints on source parameters, as shown in Table 3. These calculations were performed according to the methods described by Sobolev et al. (1997a), Sutton et al. (2001), and Salii et al. (2002), but without an incident infrared radiation field. Assuming that the warm dust is localized to the immediate vicinities of W3(OH) and W3(H_2O), the infrared field should be down by a factor of at least 500 at the positions of swA and swB, relative to that near W3(OH). The physical parameters of kinetic temperature, hydrogen density, methanol column density, and source size were varied to obtain optimal agreement between the model and the observed fluxes. Parameter uncertainties were obtained in the usual fashion (Press et al. 1992, pp. 684–694) from the curvature of the χ^2 hypersurface. Each represents a 68% confidence limit after marginalizing over the remaining parameters.

Comparing our methanol column densities with an estimated hydrogen column density of 3×10^{23} cm^{-2} for this region

TABLE 3
PHYSICAL PARAMETERS FOR CLUMPS swA AND swB AND W3(H_2O)

Source	T_{kin} (K)	n_{H_2} (cm^{-3})	$N_A + N_E$ (cm^{-2})	M_{gas} ($M_\odot$)	$(N_A + N_E)/N_{H_2}$
swA	103 ± 34	$1.4^{+1.2}_{-0.6} \times 10^5$	$3.4^{+2.3}_{-1.4} \times 10^{15}$	≈ 0.05	$3.7^{+4.4}_{-2.0} \times 10^{-7}$ [a]
swB	47 ± 6	$2.0^{+3.3}_{-1.2} \times 10^6$	$4.6^{+1.3}_{-1.0} \times 10^{15}$	≈ 1.1	$3.1^{+4.0}_{-1.7} \times 10^{-8}$ [a]
W3(H_2O)	140 ± 10	$0.9^{+2.4}_{-0.7} \times 10^7$	$(2.4 \pm 0.3) \times 10^{18}$	≈ 1.6	$5.0^{+18}_{-4} \times 10^{-6}$ [a] $1.7^{+1.3}_{-0.7} \times 10^{-6}$ [b]

NOTE.—Estimated 68% confidence limits.

[a] N_{H_2} is based on density and estimated path length. The uncertainty in the fractional abundance typically is dominated by the uncertainty in density.

[b] Estimated fractional abundance based on infrared pumping. The stated uncertainty reflects only that associated with the amount of infrared pumping and ignores uncertainties in the gas-to-dust ratio, the dust absorption coefficient, and the dust opacity law.

(Wilson et al. 1993), we derive a methanol fractional abundance of the order of 10^{-8}. Independent estimates of hydrogen column densities for the individual sources can be obtained by multiplying the hydrogen number densities from Table 3 by the thicknesses along the lines of sight (assumed to be equal to the derived source diameters of 4400 AU for swA and 5000 AU for swB). These yield methanol fractional abundances of 3.7×10^{-7} for swA and 3.1×10^{-8} for swB. These methanol fractional abundances are higher than the values of the order of 10^{-9} usually seen in dark molecular clouds (Kalenskii & Sobolev 1994). But they appear to be lower than the values of the order of 10^{-6} found for other star-forming regions (Menten et al. 1986) and generally attributed to thermal evaporation of dust grain mantles. Thermal evaporation of methanol from polar ice mantles is thought to occur at temperatures of 85–90 K (Hasegawa & Herbst 1993; van Dishoeck et al. 1993; Tielens & Whittet 1997; van Dishoeck & Blake 1998). Therefore, the higher methanol fractional abundance in swA is consistent with its higher temperature, as shown in Table 3. At the minimum projected distances of these clumps from W3(OH), neither gas nor dust grains are likely to reach temperatures of this magnitude solely as a result of the luminosity of W3(OH) (Doty & Neufeld 1997). Therefore, it is possible that swA contains an internal heating source. Since the temperature of swB is insufficient to evaporate methanol, some nonthermal desorption mechanism may be necessary to release the observed amount of methanol.

Assuming uniform densities, masses for the gas in clumps swA and swB also may be obtained, as shown in Table 3. These masses are of the order of 0.05 and 1.1 $M_\odot$, respectively, with large uncertainties that are probably dominated by uncertainties in the sizes and filling factors. These numbers may be compared with an estimate for the total mass in a larger region to the southwest of W3(OH) of 80 $M_\odot$ (Wilson et al. 1993). The observed line widths imply virial masses of the order of 25 $M_\odot$ each for swA and swB. It is unlikely that either clump is gravitationally bound, unless it contains a compact core of significant mass that remains unresolved in the current observations. A collapsing high-mass core, or a high-mass protostar at a very early evolutionary stage, in the center of swA could provide sufficient mass to bind the surrounding gas cloud, as well as the luminosity needed to produce the observed gas temperature.

For source swA, our best model fit shows that all of the lines listed in Table 2 are inverted, except for $0_0-1_{-1}E$. However, only $5_{-1}-4_0E$ and $8_0-7_1A^+$ show significant amplification, with $\tau = -0.8$ and -0.9, respectively. For source swB the energy levels are more nearly thermalized, as expected for the higher H_2 density. Although three of the lines are still inverted, only $8_0-7_1A^+$ shows significant amplification, with $\tau = -0.6$. Our model predicts that at these locations the closely related 36 GHz ($4_{-1}-3_0E$) and 44 GHz ($7_0-6_1A^+$) methanol maser lines will also be inverted and show modest amplification ($\tau \approx -1$). Higher-J members of these series exhibit weaker inversions. Observed line widths of 2.1 km s^{-1} (Haschick & Baan 1989; 36 GHz), 0.8 km s^{-1} (Haschick et al. 1990; 44 GHz), 2.1 km s^{-1} (for swA at 84.5 GHz; this work), and 2.5 km s^{-1} (for swA at 95.2 GHz; this work) are narrower than typical widths for this source (Kalenskii et al. 1997), consistent with modest amplification in these lines.

Our modeling of the southwest region gives a possible explanation for some of the complex behavior of the 25 GHz J_2–J_1E lines near W3(OH). The observations of Menten et al. (1986) showed a mixture of absorption- and emission-line components in this band when viewed with a large beam toward W3(OH). The strongest emission was seen for $J = 3$, although emission was evident up to $J = 9$. Our model of swB predicts a weak inversion in the $J = 3$ line, superthermal excitation in $J = 4$, and weak emission for other nearby values of J. In contrast, Sutton et al. (2001) predicted absorption from the material directly in front of the W3(OH) UCH II region. Since the Menten et al. (1986) beam encompassed both W3(OH) and swB, their observations showed a mixture of these characteristics, further complicated by emission and absorption from other methanol-rich regions contained within their beam (see Fig. 1*a*).

4.2. *W3*(H_2O) *Region*

Most of the lines studied here exhibit strong emission from the region around the water maser source W3(H_2O). Careful examination of our maps with the best signal-to-noise ratio and highest spatial resolution reveal that the bulk of the methanol emission comes from a region approximately $2''.0 \times 1''.2$ in size, elongated along a position angle of $100^\circ \pm 10^\circ$ and centered about $5''.3$ east of our nominal map center ($\Delta\alpha = 5''.3 \pm 0''.1, \Delta\delta = 0''.1 \pm 0''.1$). In other words, the emission comes from a region encompassing the TW object (Turner & Welch 1984) and continuum peaks B and C of Wyrowski et al. (1999).

This is illustrated in Figure 4, which presents a $0''.6$ resolution map of the 1.3 mm continuum from this region. Sources A (the TW object), B, and C of Wyrowski et al. (1999) are labeled. Our continuum map has slightly lower resolution than that of Wyrowski et al., and we do not resolve their sources B and C from each other. A solid line is overlaid on the map to represent the elliptical region of methanol

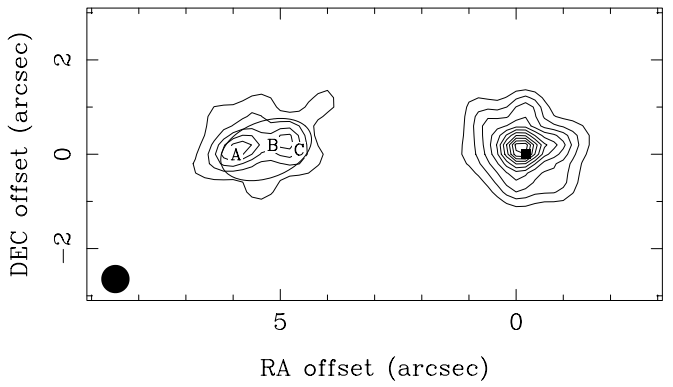

FIG. 4.—Continuum map at 1.3 mm with 0.″6 resolution. Contours are multiples of 0.1 Jy beam^{-1}. Peaks A, B, and C of Wyrowski et al. (1999) are labeled. Our measured position and positional uncertainty of the 3 mm W3(OH) continuum center are indicated by the filled box. The $2.''0 \times 1.''2$ ellipse represents our best estimate of the position and extent of the region of methanol emission near W3(H_2O).

emission described above. The extent of the methanol emission roughly corresponds to the 0.2 Jy beam^{-1} contour of the continuum map. The similarity in position, size, shape, and orientation of the methanol and the continuum emission strongly suggests they are coming from the same material. We note that the agreement in position can be made even better by shifting the 1.3 mm continuum map south 0.″1 and west 0.″1. Such a shift is within the estimated positioning error of our map and also serves to shift the center of the W3(OH) 1 mm continuum onto our previously reported 3 mm position (Sutton et al. 2001), as shown in Figure 4. It also brings our two W3(H_2O) peaks into better agreement with peak A and an average of peaks B and C of Wyrowski et al. (1999).

In Table 4 we present the observed integrated line fluxes for these lines, and in Figure 5*a* we plot these fluxes versus upper-state energies in the usual "rotation diagram" format. The diagram assumes a source solid angle of $\Omega = 4.4 \times 10^{-11}$ sr, a value that gives the optimal fit in the procedure described below. In the limit of optically thin emission from a region in LTE, the points in a rotation diagram should fall on a straight line, with the slope indicating the kinetic temperature and the intercept containing information about the total column density, according to the relations

$$\frac{N_u}{g_u} = \frac{3c^2}{16\pi^3\nu^3}\frac{1}{\Omega}\frac{\int S_\nu\, dv}{\mu^2 S}$$

and

$$\frac{N_u}{g_u} = \frac{N_T}{Q(T_{\rm rot})} e^{-E_u/kT_{\rm rot}}.$$

In these equations the total column density, N_T, and the upper-state column density divided by the level degeneracy, N_u/g_u, are averages over the source solid angle, Ω. The rotational partition function is $Q(T_{\rm rot})$, and the vibrational partition function is neglected. The observed flux integrated over velocity is $\int S_\nu\, dv$. The energy of the upper state is E_u, and the square of the dipole moment matrix element for the transition is $\mu^2 S$. Values for both are given in Table 1. The other symbols take on their usual meanings. The data show large deviations from straight-line behavior, indicating the breakdown of one or more of the assumptions implicit in the rotation diagram technique. Several of the lines shown are, in fact, optically thick. In a rotation diagram, optically thick lines appear artificially low, since the observed intensity is less than that expected from a linear extrapolation from the optically thin regime. The optical depth of a line in LTE is given by

$$\tau = \frac{8\pi^3}{3h}\mu^2 S \frac{N_0}{g_0} e^{-E_u/kT_{\rm rot}}\left(e^{h\nu/kT_{\rm rot}} - 1\right)\frac{1}{\Delta v},$$

where Δv is the line width and N_0/g_0 is the column density of the ground state. The optical depths of these lines range from 0.1 to 4.6, with approximately half of the lines showing significant saturation. The effects of saturation may be corrected using the factor C_τ (Goldsmith & Langer 1999; Gibb et al. 2000), where

$$C_\tau = \frac{\tau}{1 - e^{-\tau}}.$$

In Figure 5*b* we present a "corrected" rotation diagram, in which the deviations from straight-line behavior are much reduced. It is apparent that the largest deviations in the original diagram were the result of saturation. The best fit in Figure 5*b* has an intercept of $N_0/g_0 = 1.3 \times 10^{15}$ cm^{-2}, a slope corresponding to a rotational temperature of 149 K, and a solid angle of 4.4×10^{-11} sr. This gives a value of $\chi^2 = 128$ for 35 degrees of freedom (38 data points minus 3 free parameters). Some significant deviations from a good fit still remain, so the next step is to determine whether they represent real departures from LTE.

A non-LTE environment in which collisional pumping dominates over radiative excitation produces conditions similar to those in Class I methanol masers. Under these conditions, certain lines are predicted to have superthermal excitation, particularly those with upper states in the $K = -1$ *E*- and $K = 0$ *A*-ladders. Four out of the five such lines in this data set lie above the average trend of the data in Figure 5*b*. Similarly, *b*-type lines with lower states in these ladders are predicted to show subthermal excitation. Again, four out of five such lines lie below the average trend of the data. Therefore, the conditions around W3(H_2O) appear similar to those in Class I maser regions, even though W3(H_2O) is not a methanol maser source.

We performed detailed non-LTE calculations for the data in Table 4, using a simplified model of the infrared radiation field. Such a treatment is justified, since at these densities methanol is near the collisionally dominated limit. Ostrovskii & Sobolev (2002) have shown that when the color temperature of the radiation is in the range 125–250 K, the methanol radiative excitation occurs primarily through a large number of strong methanol absorption lines in the 15–40 μm wavelength range. The most important parameter of the infrared radiation field therefore is its intensity in this band. We assume that the pumping radiation is produced by warm dust intermixed with the gas and at the same physical temperature as the gas. At these wavelengths the dust is optically thick in this source, minimizing the importance of infrared sources external to the cloud (although the TW source and Wyrowski's sources B and C remain the ultimate sources of energy in this region).

Methanol radiative transition rates were taken from Mekhtiev et al. (1999). Collisional transition rates were based on the model of Peng & Whiteoak (1993). For simplicity, a λ^{-2} dust opacity law was chosen. Details of the excitation do depend on the optical properties of the dust grains (Ostrovskii & Sobolev 2002), but the differences are small at high gas densities. Radiative transfer for the millimeter-wavelength

TABLE 4
INTEGRATED FLUXES FROM W3(H_2O)

TRANSITION		FREQUENCY	E_u	$\int S_\nu\, dv$[a]	MODEL
Line	State	(MHz)	(K)	(Jy km s^{-1})	(Jy km s^{-1})
7_2–8_1A^-		80,993.26	103	3.5 ± 0.4	3.7
13_{-3}–$14_{-2}E$		84,423.71	274	2.2 ± 0.2	2.5
5_{-1}–4_0E		84,521.21	40	7.2 ± 0.7	7.1
6_{-2}–$7_{-1}E$		85,568.07	75	5.6 ± 0.6	4.7
7_2–6_3A^-		86,615.60	103	3.3 ± 0.3	3.0
7_2–6_3A^+		86,902.95	103	2.8 ± 0.3	3.1
8_{-4}–$9_{-3}E$		89,505.78	171	3.1 ± 0.4	3.1
1_0–2_1E	$v_t = 1$	93,196.66	303	1.8 ± 0.2	1.3
8_3–9_2E		94,541.81	131	4.8 ± 0.5	5.0
8_0–7_1A^+		95,169.52	84	11.5 ± 1.2	8.6
2_1–1_1A^+	$v_t = 1$	96,396.06	332	1.4 ± 0.2	1.0
2_1–1_1E	$v_t = 1$	96,492.16	298	1.7 ± 0.2	1.3
2_0–1_0E	$v_t = 1$	96,493.55	308	2.0 ± 0.2	1.6
2_{-1}–$1_{-1}E$	$v_t = 1$	96,501.70	420	0.8 ± 0.2	0.6
2_0–1_0A^+	$v_t = 1$	96,513.67	431	0.7 ± 0.2	0.7
2_1–1_1A^-	$v_t = 1$	96,588.59	332	1.3 ± 0.2	1.0
2_{-1}–$1_{-1}E$		96,739.36	12.5	6.8 ± 0.7	6.4
2_0–1_0A^+		96,741.38	7.0	9.2 ± 0.9	7.2
2_0–1_0E		96,744.55	20	8.1 ± 0.8	7.1
2_1–1_1E		96,755.51	28	6.8 ± 0.7	6.1
6_1–5_0E	$v_t = 1$	99,730.96	340	2.4 ± 0.4	2.5
13_2–12_3E		100,638.87	234	4.5 ± 0.5	5.6
13_{-3}–$12_{-4}E$		104,060.72	274	2.3 ± 0.8	3.7
11_{-1}–$10_{-2}E$		104,300.40	159	6.8 ± 0.7	7.7
13_{-2}–13_1E		104,336.64	237	3.4 ± 1.1	2.4
10_4–11_3A^-		104,354.86	208	3.7 ± 0.8	4.4
10_4–11_3A^+		104,410.49	208	3.4 ± 0.6	4.4
13_1–12_2A^+		105,063.76	224	7.1 ± 0.7	7.3
14_{-2}–14_1E		105,576.39	270	3.2 ± 0.3	2.8
3_1–4_0A^+		107,013.81	28	7.5 ± 0.8	9.9
15_{-2}–15_1E		107,159.92	305	3.6 ± 0.4	3.3
0_0–$1_{-1}E$		108,893.93	13.1	6.9 ± 0.7	7.3
14_5–15_4E		109,138.69	380	4.3 ± 0.8	2.9
16_{-2}–16_1E		109,153.21	342	3.6 ± 0.4	3.5
7_2–8_1A^+		111,289.60	103	8.1 ± 0.8	8.1
5_1–4_2E		216,945.56	56	28.0 ± 7.0	37.8
6_1–7_2A^-	$v_t = 1$	217,299.16	374	15.5 ± 3.9	24.2
8_0–7_1E		220,078.49	97	41.4 ± 10.4	47.6

[a] Integrated over the velocity range from −54 to −44 km s^{-1}.

methanol lines was treated using the large velocity gradient (LVG) approximation. Further details regarding the calculational methods may be found in Köppen & Kegel (1980), Sobolev (1982), and Sobolev et al. (1997a, 1997b).

The gas cloud was assumed to be uniform in H_2 density, gas and dust temperature, dust-to-gas ratio, and methanol fractional abundance. The data were not adequate to justify a more complicated, spatially inhomogeneous model of the cloud. The source solid angle was fixed at 4.4×10^{-11} sr, as given above. The other four parameters were allowed to vary. An optimal fit for W3(H_2O) was obtained with a kinetic temperature of 140 ± 10 K, hydrogen density of $0.9^{+2.4}_{-0.7} \times 10^7$ cm^{-3}, and $N_A + N_E = (2.4 \pm 0.3) \times 10^{18}$ cm^{-2}, as shown in Table 3. We can multiply the hydrogen number density by the estimated source thickness of 3400 AU to derive a hydrogen column density. Combining this with the measured methanol column density gives a methanol fractional abundance of the order of 5×10^{-6} for W3(H_2O). In comparison with the values in Table 3, van der Tak et al. (2000b) give a kinetic temperature of greater than 200 K for W3(H_2O) from statistical equilibrium calculations for H_2CO, similar to those given earlier by Helmich et al. (1994) and Helmich & van Dishoeck (1997). However, the beam size for those observations was large enough to encompass W3(OH) as well as W3(H_2O). The methanol column density of van der Tak et al. (2000a) is smaller than that given in Table 3, an effect we also attribute to their larger beam size. The density profile of van der Tak et al. (2000b) corresponds to a density of about 3×10^7 cm^{-3} at a characteristic radius of 2000 AU, consistent with our result.

The observations also provided good constraints on the amount of dust needed in the model. This gives us an independent method to calculate the hydrogen column density and derive a methanol fractional abundance. Previously, we adopted a λ^{-2} dust opacity law. Now, only for the purpose of this calculation, we further adopt a gas-to-dust mass ratio of 100 and a dust mass absorption coefficient of 1.1 cm^2 g^{-1} at 1.3 mm (Henning et al. 1995). This yields a methanol fractional abundance of the order of 1.7×10^{-6} for W3(H_2O). Given the uncertainties inherent in these various assumptions,

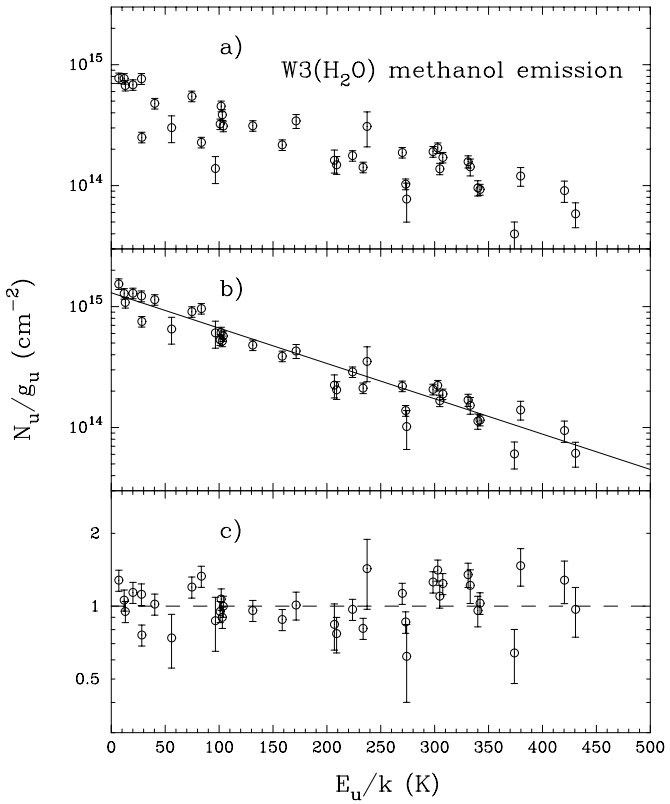

FIG. 5.—Rotation diagram fit to methanol emission from W3(H_2O). In (*a*) the ordinate is $3c^2 \int S_\nu \, dv/(16\pi^3\nu^3\Omega\mu^2 S)$. In (*b*) the ordinate is the above quantity times C_τ, i.e., corrected for optical depth. The solid line is for the best weighted χ^2 fit to the data and gives a rotational temperature of 149 K and $N_0/g_0 = 1.3 \times 10^{15}$ cm^{-2}. In (*c*) the ordinate is the ratio of the observed integrated flux to that predicted by the non-LTE model discussed in the text.

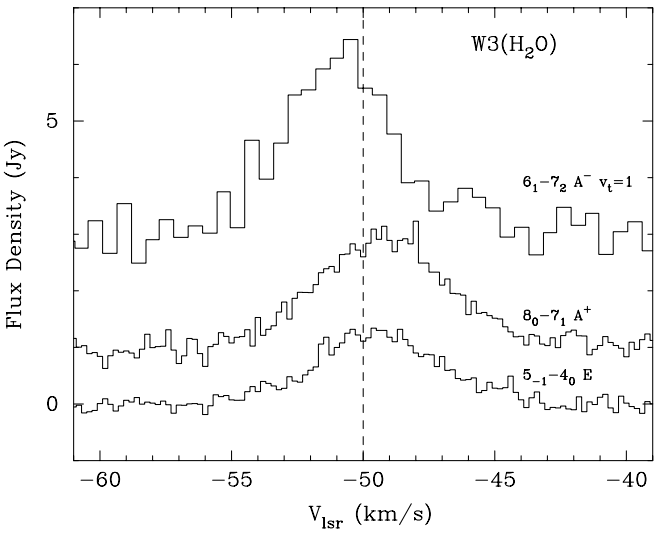

FIG. 6.—Spectra of three lines from a $4'' \times 4''$ region around the center of W3(H_2O), offset by ($\Delta\alpha = +5''.3$, $\Delta\delta = +0''.1$) from the reference position.

the two estimates of the fractional abundance agree well and support the notion of significant grain evaporation in this source.

Figure 5*c* shows the residuals from the optimal non-LTE fit. For this fit $\chi^2 = 86$ for 34 degrees of freedom (38 data points minus 4 free parameters). The non-LTE model is a significantly better fit to the data than the LTE model. There are still some significant residuals, possibly indicating that the observational uncertainties were underestimated. But it should be kept in mind that there are additional uncertainties, those associated with the model calculations. Such uncertainties are difficult to quantify, but they appear to be of the same order as those associated with the observations. The nature of these uncertainties is discussed in Appendix B of Sutton et al. (2001). The dominant uncertainty may be spatial variation in the source parameters.

The results presented above are based on averages over the entire W3(H_2O) source. Although our spatial resolution is generally insufficient to resolve the TW object from sources B and C of Wyrowski et al. (1999), we do have some information on spatial substructure from the shape of the spectra. For the 29 $v_t = 0$ lines listed in Table 1, the average methanol emission velocity toward W3(H_2O) is -50.0 km s^{-1}, with a standard deviation of 0.37 km s^{-1} (giving a standard error of the mean of less than 0.1 km s^{-1}). Several lines with good signal-to-noise ratios show distinct shifts from this velocity, as shown in Figure 6. The $6_1-7_2A^-$ $v_t = 1$ line is well fitted by a single Gaussian with a velocity of -51.0 ± 0.1 km s^{-1}. This blueshifted emission is more characteristic of the TW source in the eastern part of W3(H_2O). Note that in Figure 3*o*, the emission peak for this line is spatially coincident with the TW object. This is a high-excitation line ($E_u = 374$ K), presumably more easily excited close to the main source of luminosity in the region, namely, the TW object. The $8_0-7_1A^+$ and $5_{-1}-4_0E$ lines have mean velocities of -49.3 ± 0.1 and -49.5 ± 0.1 km s^{-1}, respectively. Redshifted emission is characteristic of the western portion of W3(H_2O), near Wyrowski's source C. And in the maps of these lines, the emission peaks distinctly to the west of TW (Figs. 1*e* and 1*f*—although this shift to the west is too small to be seen on the scale at which these maps are presented). So the data suggest that the line-of-sight velocity difference between the TW object and source C may be of the order of 1.6 km s^{-1}. The $8_0-7_1A^+$ and $5_{-1}-4_0E$ lines are the same two lines discussed in § 4.1, known elsewhere for their Class I methanol maser emission. Since such lines are known to be collisionally pumped, the luminosity source proposed by Wyrowski et al. (1999) may either be sufficiently weak or sufficiently well shielded from the methanol-rich material for collisional pumping to dominate. We should note that in our non-LTE model for the W3(H_2O) region, these two lines are optically thick, with opacities of $\sim$3.7 and $\sim$1.6, respectively. So we may be seeing a preponderance of foreground material in these lines.

Given a density of 0.9×10^7 cm^{-3} and assuming that W3(H_2O) is as deep along the line of sight as its average extent in the plane of the sky (3400 AU), this corresponds to 1.6 $M_\odot$ of warm gas, excluding that contained in protostellar-sized objects and condensed cores. This may be compared with a previous estimate of the gas mass of "at least a few $M_\odot$" (Turner & Welch 1984). The estimate of 70 $M_\odot$ by Wilson et al. (1991) refers to a considerably larger region (0.13 pc) probed by $C^{18}O$. Wink et al. (1994) estimate 60 $M_\odot$ in a 0.05 pc diameter region from $C^{18}O$ observations; however, they also estimate 30 $M_\odot$ on a 0.01 pc scale from dust observations. Finally, Wilson et al. (1993) give a dynamical mass of 18 $M_\odot$, which therefore includes that of any protostars.

Nonthermal continuum emission at centimeter and decimeter wavelengths has been seen both east and west of the

TW object (Reid et al. 1995; Wilner et al. 1999; Argon et al. 2003). This has been interpreted as synchrotron radiation from precessing jets (Wilner et al. 1999), in part due to the symmetry and curvature of the emission and its location near the apparent center of expansion of the H_2O masers. However, alternative explanations are possible. Torrelles et al. (2002) point out that in some cases of star formation, water masers are found in protoplanetary accretion disks, oriented perpendicular to the radio jet directions (although Torrelles et al. 2002 do not consider the TW object to be such a system). But recently, Shchekinov & Sobolev (2004) have proposed a model in which the H_2O masers in W3(H_2O) are formed on the surface of an east-west circumstellar disk or ring.

This question of orientation has some bearing on the nature of the object we have been calling Wyrowski's source C. Its location is along the east-west axis of the synchrotron jet proposed by Reid et al. (1995). In fact, it is roughly coincident with the cluster of water masers located 1″ west of the TW object. Since jets produce shocks where they run into ambient material, and shocks, in turn, can power masers, one possibility is that Wyrowski's source C is a deeply embedded Herbig-Haro object. However, Wilner et al. (1999) and Wyrowski et al. (1999) agree that regardless of jet geometry, the most likely interpretation is that Wyrowski's source C is a deeply embedded protostellar object. We concur.

Using this interpretation and assuming that the molecular gas seen in methanol is roughly equally divided between the TW object and Wyrowski's source C, we get the following picture. The TW object itself is a protostar of about 15 $M_\odot$ (Mauersberger et al. 1988). Wyrowski's sources B and C may contain additional protostellar cores of similar or smaller mass (Wyrowski et al. 1999). Within 0.01 pc of each of these sources there is about 1 $M_\odot$ of warm gas. And on larger scales, there are an additional few tens of solar masses of cooler, less dense gas.

The dynamical stability of such a system is uncertain. The putative sum of the protostellar masses (20–30 $M_\odot$), the projected separation (≈2500 AU), and the estimated line-of-sight velocity difference (1.6 km s^{-1}) are consistent with a reasonable binary orbit of the TW object with Wyrowski's B and C. For example, a low-eccentricity, high-inclination, intermediate-phase (an angle of the order of 45° with respect to the line of nodes) orbit is consistent with the above values. This assumes that the 1.6 km s^{-1} velocity difference discussed above in connection with Figure 6 represents the true difference in line-of-sight protostellar velocities. This would be the case if each protostellar object were accompanied by its own circumstellar material, but not necessarily the case if they were orbiting within a common, circumbinary envelope. A numerical simulation by Turner et al. (1995) produces a binary system with circumstellar material in the form of individual protostellar disks, a possible case of the system described above. Lubow & Ogilvie (2000) indicate that individual disks of sufficient size, like those of Turner et al. (1995), can be stable in binary systems. The full width to zero-power line widths seen here are 10–12 km s^{-1}. Such velocities could be produced by slow infalls or outflows or by orbital motion in individual circumstellar envelopes. A significant amount of circumbinary material is also possible, although if it is in purely orbital motion it could not account for the full widths of these lines.

In a single-dish study of high-mass star–forming regions, Minier & Booth (2002) report emission from the vicinity of W3(OH/H_2O) in a number of methanol lines. They report emission peaks at −51 km s^{-1} in the $6_{-2}-7_{-1}E$ (85.5 GHz) and $7_2-8_1A^+$ (111.2 GHz) lines. Our work shows that gas at this velocity is clearly associated with the W3(H_2O) source. Minier & Booth (2002) also point out that W3(OH/H_2O) is unusual among massive star–forming regions in not displaying clear maser emission in the $8_0-7_1A^+$ (95.1 GHz) line. The emission in this line from sources swA and swB was discussed above in § 4.1 and that from W3(OH) by Sobolev et al. (2004). For the W3(H_2O) source, our model suggests an excitation temperature for this line of about 135 K and an optical depth of about 3.7, consistent with the lack of maser emission.

In our optimal non-LTE model of W3(H_2O), none of the lines studied here are inverted; excitation temperatures range from about 90 to 530 K. Optical depths of these lines range from about 0.07 to 3.9.

In our optimal non-LTE model, the lines in the $J = 2-1$ band of $^{12}CH_3OH$ have opacities ranging from 1 to 1.5. This means that, even apart from non-LTE effects, the flux ratios for the $J = 2-1$ band of $^{12}CH_3OH$ relative to $^{13}CH_3OH$ would be expected to be smaller than the actual abundance ratio by a factor of 1.9. In addition, since the $^{13}CH_3OH$ lines are optically thin, $^{13}CH_3OH$ will be more efficiently cooled, resulting in higher fractional populations in the lower rotational levels. A detailed calculation of this effect would require a larger set of $^{13}CH_3OH$ observations and a separate non-LTE model for $^{13}CH_3OH$. However, the cooling is likely to be substantial. The [^{12}C]/[^{13}C] abundance ratio is thought to be 66 ± 4 (Langer & Penzias 1990). Because of the above effects, the integrated flux ratio for the $J = 2-1$ band should be considerably smaller, possibly consistent with the observed ratio of 12 ± 3, ignoring fractionation.

5. CONCLUSIONS

To the southwest of W3(OH) there is an extensive region of gas, dense enough to be seen in a number of methanol lines. Emission is most readily seen in lines of low upper-state energy ($E_u \lesssim 15$ K) and in lines known elsewhere for their Class I methanol maser emission. In this case, strong Class I masers do not seem to be present, but the physical conditions are similar to those seen in Class I maser regions. Excitation is collisionally driven, with densities of the order of 10^5–10^6 cm^{-3}. Inverted populations and weak amplification appear to be present. We predict that the 36 and 44 GHz lines will also be inverted, although it is doubtful that their optical depths will be sufficient to produce strong masers. The region is clumpy on scales of about 1 to a few tens of solar masses. Kinetic temperatures range up to about 100 K. The warmest regions have methanol fractional abundances of the order of 10^{-7}, suggesting that some grain mantle evaporation has taken place, but that the evaporation is incomplete.

In contrast, toward W3(H_2O) the methanol emission is nearly thermalized and many lines are optically thick. None of the lines studied have inverted populations. Excitation is due to a combination of collisional and radiative processes. The size of the methanol-emitting region is about 2600×4400 AU. This is resolved into at least two components, corresponding to the TW object and a blend of Wyrowski's B and C components. It is likely that both are massive young stellar objects. Their separation and line-of-sight velocity difference are consistent with a wide binary orbit with a period of the order

of 50,000 yr. Each source may be accompanied by circumstellar material containing of the order of 1 $M_\odot$ or less of gas. There may be as much as a few tens of $M_\odot$ of circumbinary material, although its distribution is unclear. Methanol fractional abundance in the circumstellar material is of the order of 10^{-6}, indicative of a warm environment and extensive grain mantle evaporation.

This work was supported in part by the National Science Foundation under BIMA grant AST 99-81363 and CARMA grant AST 02-28953. A. M. S., S. V. S., A. V. M., A. B. O., and I. I. Z. were supported by INTAS grant 99-1667, RFBR grant 03-02-16433, and the Russian Ministry of Education (grant E02-11.0-43). The authors thank Yuri Shchekinov for helpful discussions.

REFERENCES

Argon, A. L., Reid, M. J., & Menten, K. M. 2003, ApJ, 593, 925
Caselli, P., Hasegawa, T. I., & Herbst, E. 1993, ApJ, 408, 548
Cragg, D. M., Sobolev, A. M., Ellingsen, S. P., Caswell, J. L., Godfrey, P. D., Salii, S. V., & Dodson, R. G. 2001, MNRAS, 323, 939
Doty, S. D., & Neufeld, D. A. 1997, ApJ, 489, 122
Gibb, E., Nummelin, A., Irvine, W. M., Whittet, D. C. B., & Bergman, P. 2000, ApJ, 545, 309
Goldsmith, P. F., & Langer, W. D. 1999, ApJ, 517, 209
Haschick, A. D., & Baan, W. A. 1989, ApJ, 339, 949
Haschick, A. D., Menten, K. M., & Baan, W. A. 1990, ApJ, 354, 556
Hasegawa, T. I., & Herbst, E. 1993, MNRAS, 261, 83
Helmich, F. P., Jansen, D. J., de Graauw, Th., Groesbeck, T. D., & van Dishoeck, E. F. 1994, A&A, 283, 626
Helmich, F. P., & van Dishoeck, E. F. 1997, A&AS, 124, 205
Henning, Th., Michel, B., & Stognienko, R. 1995, Planet. Space Sci., 43, 1333
Humphreys, R. M. 1978, ApJS, 38, 309
Kalenskii, S. V., Dzura, A. M., Booth, R. S., Winnberg, A., & Alakoz, A. V. 1997, A&A, 321, 311
Kalenskii, S. V., & Sobolev, A. M. 1994, Astron. Lett., 20, 91
Köppen, J., & Kegel, W. H. 1980, A&AS, 42, 59
Langer, W. D., & Penzias, A. A. 1990, ApJ, 357, 477
Lubow, S. H., & Ogilvie, G. I. 2000, ApJ, 538, 326
Mauersberger, R., Wilson, T. L., & Henkel, C. 1988, A&A, 201, 123
Mekhtiev, M. A., Godfrey, P. D., & Hougen, J. T. 1999, J. Mol. Spectrosc., 194, 171
Menten, K. M., Walmsley, C. M., Henkel, C., & Wilson, T. L. 1986, A&A, 157, 318
Minier, V., & Booth, R. S. 2002, A&A, 387, 179
Nilsson, A., Bergman, P., & Hjalmarson, Å. 2000a, A&AS, 144, 441
Nilsson, A., Hjalmarson, Å., Bergman, P., & Millar, T. J. 2000b, A&A, 358, 257
Ostrovskii, A. B., & Sobolev, A. M. 2002, in IAU Symp. 206, Cosmic Masers: From Protostars to Black Holes, ed. V. Migenes & M. J. Reid (San Francisco: ASP), 183
Peng, R. S., & Whiteoak, J. B. 1993, MNRAS, 260, 529
Press, W. H., Teukolsky, S. A., & Vetterling, W. T., & Flannery, B. P. 1992, Numerical Recipes in FORTRAN77: The Art of Scientific Computing (2nd ed.; Cambridge: Cambridge Univ. Press)
Reid, M. J., Argon, A. L., Masson, C. R., Menten, K. M., & Moran, J. M. 1995, ApJ, 443, 238
Salii, S. V., Sobolev, A. M., & Kalinina, N. D. 2002, Astron. Rep., 46, 955
Shchekinov, Yu. A., & Sobolev, A. M. 2004, A&A, 418, 1045
Slysh, V. I., Kalenskii, S. V., & Val'tts, I. E. 1993, ApJ, 413, L133
Sobolev, A. M. 1982, Soviet Astron., 26, 366
Sobolev, A. M., Cragg, D. M., & Godfrey, P. D. 1997a, A&A, 324, 211
———. 1997b, MNRAS, 288, L39
Sobolev, A. M., Cragg, D. M., Salii, S. V., Kalinina, N. D., & Ellingsen, S. P. 1998, in The Physics and Chemistry of the Interstellar Medium, ed. V. Ossenkopf, J. Stutzki, & G. Winnewisser (Herdecke: GCA), 259
Sobolev, A. M., Sutton, E. C., & Watson, W. D. 2004, in The Dense Interstellar Medium in Galaxies, ed. S. Pfalzner, C. Kramer, C. Straubmeier, & A. Heithausen (Berlin: Springer), in press
Sobolev, A. M., et al. 2002, in IAU Symp. 206, Cosmic Masers: From Protostars to Black Holes, ed. V. Migenes & M. J. Reid (San Francisco: ASP), 166
Sutton, E. C., Sobolev, A. M., Ellingsen, S. P., Cragg, D. M., Mehringer, D. M., Ostrovskii, A. B., & Godfrey, P. D. 2001, ApJ, 554, 173
Tielens, A. G. G. M., & Whittet, D. C. B. 1997, in IAU Symp. 178, Molecules in Astrophysics: Probes and Process, ed. E. van Dishoeck (Dordrecht: Kluwer), 45
Torrelles, J. M., Patel, N. A., Gómez, J. F., & Anglada, G. 2002, in Rev. Mexicana Astron. Astrofis. Ser. Conf. 13, Emission Lines from Jet Flows, ed. W. J. Henney, W. Steffen, A. C. Raga, & L. Binette (Mexico, DF: Inst. Astron., UNAM), 108
Tsunekawa, S., Ukai, T., Toyama, A., & Takagi, K. 1995, Microwave Frequencies of the CH_3OH Molecule in the Frequency Range from 7 to 200 GHz, report for the Grant-in-aid for Scientific Research on Priority Areas (Interstellar Matter, 1991–1994) of the Ministry of Education, Science, and Culture, Japan (Toyama: Toyama Univ.)
Turner, J. A., Chapman, S. J., Bhattal, A. S., Disney, M. J., Pongracic, H., & Whitworth, A. P. 1995, MNRAS, 277, 705
Turner, J. L., & Welch, W. J. 1984, ApJ, 287, L81
Val'tts, I. E., Ellingsen, S. P., Slysh, V. I., Kalenskii, S. V., Otrupcek, R., & Voronkov, M. A. 1999, MNRAS, 310, 1077
van der Tak, F. F. S., van Dishoeck, E. F., & Caselli, P. 2000a, A&A, 361, 327
van der Tak, F. F. S., van Dishoeck, E. F., Evans, N. J., II, & Blake, G. A. 2000b, ApJ, 537, 283
van Dishoeck, E. F., & Blake, G. A. 1998, ARA&A, 36, 317
van Dishoeck, E. F., Blake, G. A., Draine, B. T., & Lunine, J. I. 1993, in Protostars and Planets III, ed. E. H. Levy & J. I. Lunine (Tucson: Univ. Arizona Press), 163
Voronkov, M. A., Austin, M. C., & Sobolev, A. M. 2002, A&A, 387, 310
Wilner, D. J., Reid, M. J., & Menten, K. M. 1999, ApJ, 513, 775
Wilson, T. L., Gaume, R. A., & Johnston, K. J. 1993, ApJ, 402, 230
Wilson, T. L., Johnston, K. J., & Mauersberger, R. 1991, A&A, 251, 220
Wink, J. E., Duvert, G., Guilloteau, S., Güsten, R., Walmsley, C. M., & Wilson, T. L. 1994, A&A, 281, 505
Wyrowski, F., Schilke, P., Walmsley, C. M., & Menten, K. M. 1999, ApJ, 514, L43
Xu, L.-H., & Lovas, F. J. 1997, J. Phys. Chem. Ref. Data, 26, 17